

Bridging electrode preparation and electrocatalyst performance with physics-based causal AI

Evelyna Wang¹, Linda Hung¹, Sam Witty^{1*},
Michaela Burke Stevens^{1*}, Kevin Tran^{1*}

¹Energy & Materials, Toyota Research Institute, 4440 El Camino Real,
Los Altos, 94022, CA, United States of America.

*Corresponding author(s). E-mail(s): sam.witty@tri.global;
michaela.stevens@tri.global; kevin.tran@tri.global;

Contributing authors: evelyna.wang@tri.global; linda.hung@tri.global;

Abstract

State-of-the-art artificial intelligence (AI) and Machine-Learning (ML) tools have not yet enabled rapid design of next-generation materials. Detailed physical understanding of how material properties affect device performance is required to advance materials development. For example, optimization of ink parameters for electrocatalysts has no known physical mathematical model and thus insights are difficult to translate from material studies to device studies. Herein, we demonstrate how to use the emerging AI tool, **physics-based structural causal models (SCMs)**, to extract quantitative causative insights from complex heterogeneous electrochemical systems with small ($n < 10$), but multi-modal datasets (modes > 10). Our SCM quantitatively separates the role that varying the support-to-catalyst ratios and total material loadings plays on catalytic performance. The proof of concept model developed in this work enables root-cause-analysis on the cyclic voltammograms of manganese-antimony oxide oxygen reduction electrocatalysts on Vulcan carbon supports tested in alkaline media using a rotating disc electrode device configuration. Our preliminary causal analyses quantitatively disentangle how the catalyst performance is affected by the number of active sites versus the thickness of the electrode. To the best of our knowledge, this is the first demonstration of physics-based SCMs applied to electrochemical materials and their performance.

Keywords: causal reasoning, multiscale modeling, electrocatalysis, oxygen reduction catalysis

1 Introduction

The rapid development of industrially relevant new catalysts is limited by the complexity of materials, e.g. catalysts, supports, membranes etc., and their interactions within devices. Fundamental studies focus on “well defined” catalyst systems to understand isolated catalyst properties [1–4]. One common method for quickly evaluating electrocatalysts is to use a rotating disc electrode (RDE), which has well studied mass transport, requires minimal material for testing, and is nominally inexpensive [5–7]. This method is often employed for hydrogen fuel cell catalysts, which catalyze oxygen reduction and hydrogen oxidation reactions (ORR, HOR) [8]. The typical protocol for analyzing RDE experiments and comparing catalytic performance is to fit measured voltammograms with standard physical equations, namely the Levich, the Butler-Volmer (Tafel approximation), and the Koutecký-Levich (K-L) equations [9, 10]. The Levich and K-L equations were developed to decouple the mass transport and kinetics in planar electrodes, where O_2 transport is governed by simple boundary layer diffusion with thickness determined by rotation rate [11, 12]. Parameters extracted from the fits are used to assess and compare electrocatalytic activity, including exchange current densities, selectivities, charge transfer coefficients, and limiting current densities.

Although practical catalysts in fuel cells are typically nanoparticles rather than planar surfaces, performance evaluation of nanoparticle catalysts typically use RDE experiments. The planar assumption may result in overestimation or underestimation of actual electrocatalytic effects of catalyst nanoparticles [13, 14]. Furthermore, isolating electrocatalyst properties is challenging due to the complexity of electrode design, whereby formulations of inks containing the catalyst, support, and ionomer all affect electrode properties and subsequent electrochemical performance [15–19]. Despite many useful improvements to modeling electrocatalysts in RDEs with modifications to the physical equations [20–22], as well as applying interpretable machine-learning [23], it remains challenging to disentangle the effects of different electrode components or electrode design on electrochemical performance and apply modeling results experimentally. As such, thus far, RDE evaluation of catalysts remains difficult to translate to larger scale devices (such as membrane electrode assemblies) and use in hydrogen fuel cells [5, 24–28].

New methods are needed to disentangle confounded effects of individual electrode components on experimental results. One such method is to use Structural Causal Models (SCMs), which are used to quantify root causes and disentangle complex phenomena and provide the basis for causal AI that can help resolve limitations in

conventional ML tools [29, 30]. In brief, SCMs provide a mathematical and computational scaffolding for expressing assumed cause-and-effect relationships, plus methods to identify and understand causal conclusions. SCMs have been typically employed in the social sciences, to examine cause-effect relationships [31, 32]. More recently, SCMs have been applied to materials science to analyze complex experimental datasets connecting synthesis parameters and atomic structures to material properties (e.g., graphene oxide nanoflakes, perovskites) [33–36]. In many of these settings, causal assumptions are expressed solely in terms of causal structure ($x \rightarrow y$ indicates that x causes y) rather than the specific causal mechanisms (*how* x causes y). In this work we instead use “Bayesian parametric structural causal models” [37], which express causal assumptions as a system of one-way equations —e.g., $y \leftarrow m \times x + b$. These one-way equations are well-aligned with physics-based modeling, where the Levich equation for modeling RDE experiments becomes $j_{lim} \leftarrow 0.62nFD^{2/3}\omega^{1/2}\nu^{-1/6}C_{bulk}$, where diffusivity, concentration, and rotation rates *cause* a limiting current density. The inclusion of specified causal mechanisms (inductive bias) enables the use of small experimental datasets. Along the theme of ML accelerated physics-based models [38], we set out to demonstrate the integration of physics-based equations into a structural causal model, thereby enabling systematic causal reasoning (decoupled root cause analysis) on complex electrode design parameters grounded in well established physics.

As a method proof-of-concept, we applied structural causal modeling to quantitatively probe the relationship between support ratio, total material mass loading, and electrocatalyst performance based on the experimental dataset from Kreider et al. that probes MnSb_2O_6 catalysts on Vulcan carbon supports for the ORR in alkaline media using an RDE [15]. Our SCM quantitatively connects their small ($N \sim 10$) but multi-modal dataset including experimental conditions, compositional information, in situ (double layer capacitance) and ex situ (gas adsorption) surface area measurements, atomic density, density functional theory calculations, and cyclic voltammograms (CVs). Specifically, we use our SCMs to answer the questions: *how does changing the catalyst-to-support ratio and the total material loading affect the total current density measured from voltammetry? Can we decouple the change through electrode thickness versus a change in the total number of active sites? More broadly, when changing a material or processing parameter, why does performance change?* Due to the generality of this broader question, this work explains in detail the model construction, validation, and causal query analyses with respect to the dataset used but is applicable to any electrochemical system. Our methodological results explaining the application of SCMs are detailed in the [Methods](#). Overall, this work demonstrates physic-based

SCMs and new insights for electrochemical devices that bridging material properties to device performance.

2 Results

2.1 Building a structured causal model for ORR

We constructed a **structural causal model (SCM)** of an RDE system to disentangle the effects of composite electrode properties on electrochemical performance. The SCM comprises causal relationships between catalyst properties, electrode properties, device settings, and electrochemical performance and reflects the experimental design from Kreider et al. [15], as shown in Figure 1a. The graphical representation of the full SCM is shown in Figure 1b, where all the variables within our model are represented as **nodes** and directed **edges** between nodes represent causal relationships. We refer to the model in Figure 1b as the classic planar SCM given that the planar assumptions in the Levich equation. A list of all nodes in the SCM is included in Table S1; nodes can be experimental controls and measured values as well as latent variables that are difficult to measure (which we denote as [fitted]). Nodes without incoming edges are root nodes, and typically represent experimental controls or intrinsic material properties, which will have no upstream causes.

An example of the causal relationships represented in our SCM is the directed edge connecting the cathodic charge transfer coefficient node to the kinetic current density node ($\alpha \rightarrow j_k$), which indicates that a change in α causes a change in j_k . This cause-and-effect is part of the Butler-Volmer mechanism. A change in j_k then causes a change in the measured total current via the Koutecký–Levich equation ($j_k \rightarrow j$). The full SCM as shown in Figure 1b assembles the Levich, Butler-Volmer, and the K-L equations together with additional causal relationships between the electrode engineering properties (mass loadings), catalyst properties (adsorbate binding energy, specific surface area), and electrode properties. These include conversion equations (mass and geometric area cause the normalized mass loadings), empirical relationships (Sabatier principle-based volcano relationships - adsorbate binding energy value causes a turnover frequency), as well as estimated relationships (Echem surface area catalyst and Echem surface area support sum to give Total Echem surface area). Table S1 and Figure S1 both show the full list of equations and default values for root nodes. Further discussion on the structure, directionality, and causality when translating physical equations into the causal modeling framework is included in the [Methods](#).

A [Glossary of terms](#) is also included due to the interdisciplinary nature of developing causal models for electrochemical experiments.

Experiment ID	Total material loading (MnSb ₂ O ₆ + Vulcan carbon)	Support to catalyst ratio	Normalized Catalyst loading (MnSb ₂ O ₆)
A	0.27 mg*cm ⁻²	0.09	0.25 mg*cm ⁻²
B	0.31 mg*cm ⁻²	0.2	0.25 mg*cm ⁻²
C	0.38 mg*cm ⁻²	0.33	0.25 mg*cm ⁻²
D	0.44 mg*cm ⁻²	0.43	0.25 mg*cm ⁻²
E	0.125 mg*cm ⁻²	0.2	1.0 mg*cm ⁻²
F	0.625 mg*cm ⁻²	0.2	0.5 mg*cm ⁻²
G	1.25 mg*cm ⁻²	0.2	1.0 mg*cm ⁻²
H	0.625 mg*cm ⁻²	0.09	0.57 mg*cm ⁻²
I	0.625 mg*cm ⁻²	0.33	0.41 mg*cm ⁻²

Table 1 Summary of the experiment set we analyzed and used for model training. Each of the experiments will correspond with an experiment plate in the SCM shown in Figure 1b; see [Translating experimental workflows and physical equations into SCMs](#) for further discussion.

Once the classic planar SCM was constructed, simulated voltammograms were compared to experimental data to assess preliminary model accuracy, see Figure S2. We refer to these simulations from the model *before* training with data as **prior distributions**. The model was then trained on all the experimental data from Kreider et al. (Table 1). During training, the prior distributions of the latent variables in the model are updated in order to better match distributions for nodes with data to the measured data values, producing approximate **posterior distributions**. This fitting process is conceptually similar to what is commonly called “learning” or “fitting” parameters in standard ML or physical models, however, in our Bayesian SCMs the result is a set of distributions rather than scalar, vector, or tensor values. Nodes labeled as “fitted” are attributed with distributions (via kernels; see [Methods](#)) and updated during training (see Table S1). The list of all applied uncertainty distributions in the model and rationale are included in Table S1. To note, the Bayesian SCM framework we implemented incorporates probabilistic methods when modeling uncertainty and training.

For nodes with experimental data that we are trying to predict, namely the total current density, we compared the model posterior distribution with the data. The purple band shown in Figure 2a is the posterior distribution for the experiment-specific

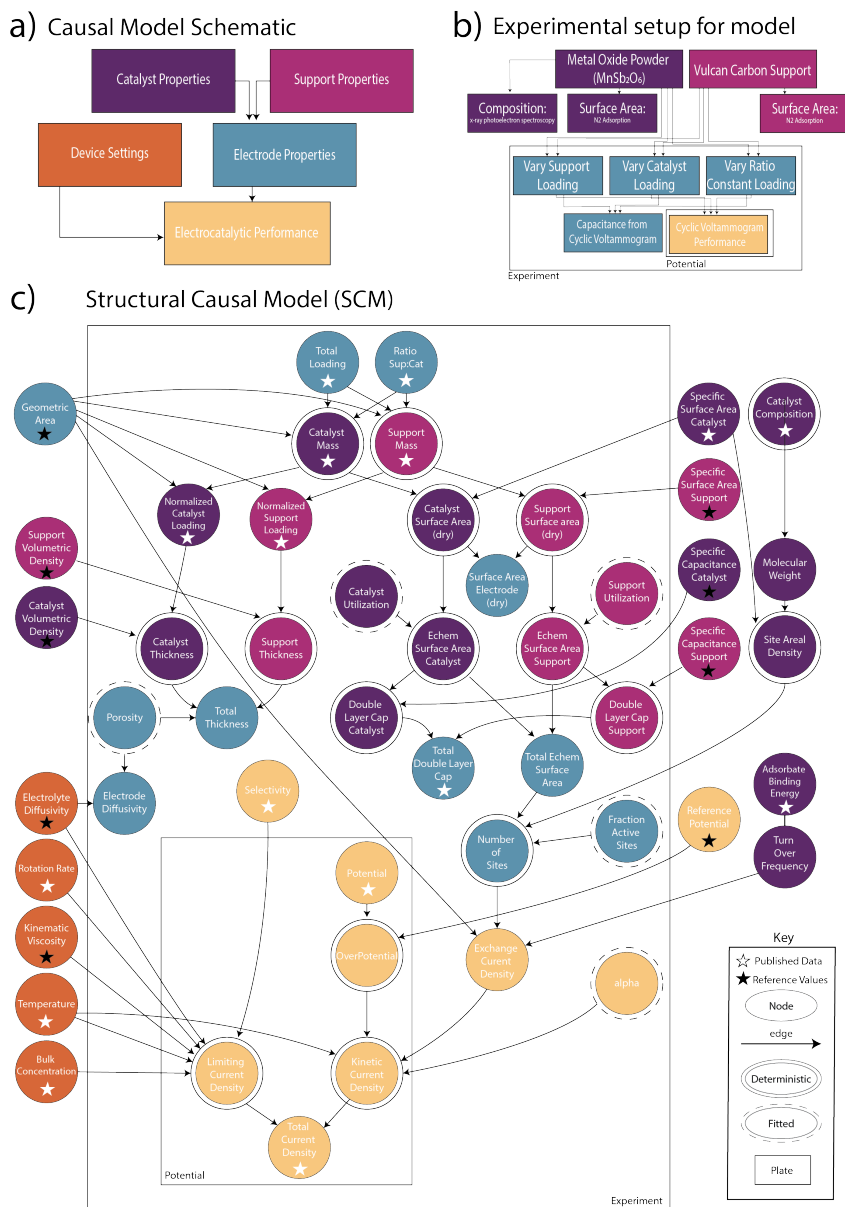


Fig. 1 a) A schematic that shows how catalyst and support properties influence electrode properties. The electrode and device settings are input causes into the electrocatalytic performance, which encompasses the Levich, Butler-Volmer, and Koutecky-Levich equations, b) a schematic that blocks the experimental design and workflow into causal relationships, including multi-modal characterization and different experiments varying support and catalyst ratios that then cause the electrocatalytic performance for the cyclic voltammetry measurement, and c) the full classic planar SCM constructed is shown in detail. Nodes labeled with a white star denote experimental data from Kreider et al. and nodes with black star denote literature data or reference values used. Nodes that are deterministically calculated have also been labeled as well as nodes that are fitted during training. Edges represent directional causal relationships between nodes. There is additional structural information depicted by the nested plating structures, which represent repeated elements in the model, such as the cyclic voltammogram in the potential plate or each individual support ratio/loading in the experimental plate (see [Translating experimental workflows and physical equations into SCMs](#) for further discussion).

voltammogram. For comparison, the standard procedure of fitting the Levich, Butler-Volmer, and the K-L equations to experimental data is shown in Figure 2b. Both these fittings were done with global charge transfer coefficients.

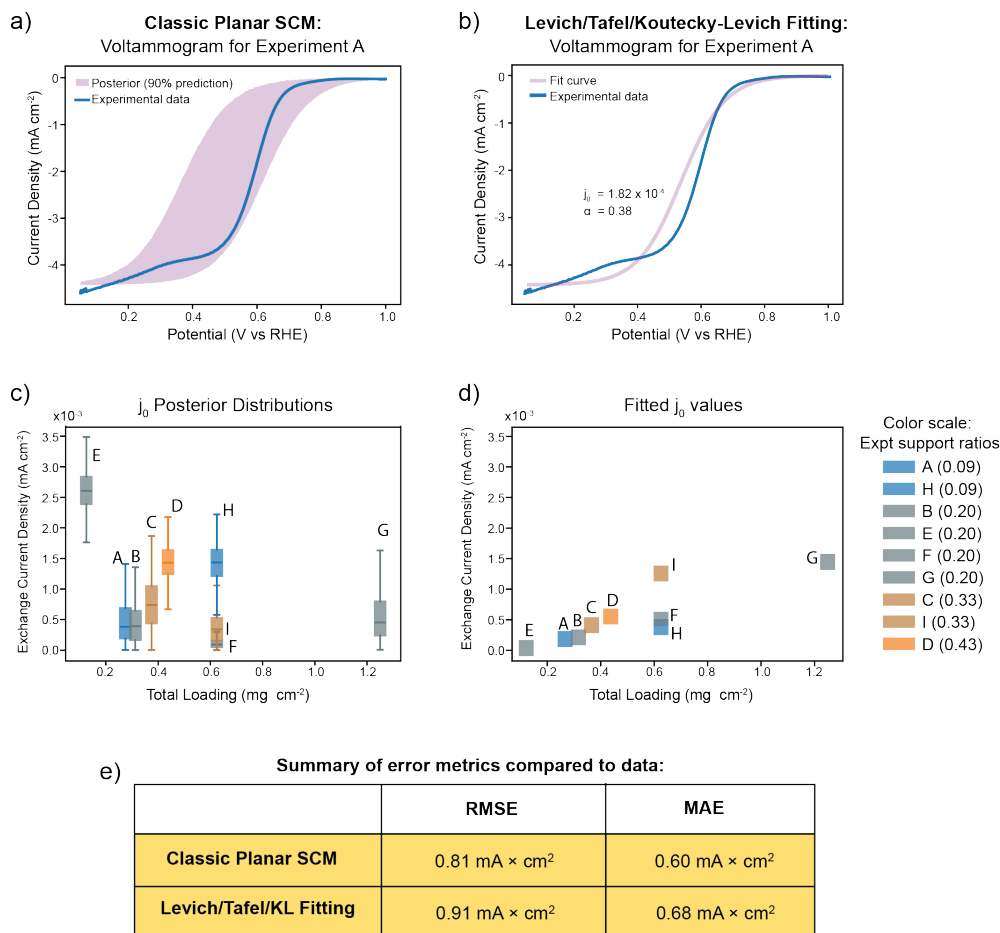


Fig. 2 The simulated voltammogram from a) the classic planar model or b) the fit line from Levich/Tafel/KL equation fitting for the reverse sweep of oxygen reduction cyclic voltammogram of MnSb_2O_6 on Vulcan carbon using an RDE, Experiment A [total loading = $0.27 \text{ mg} \cdot \text{cm}^{-2}$ and support ratio = 0.09]. Resulting posterior distributions for the exchange current density from c) classic planar SCM and resulting fitted exchange current densities from d) conventional experimental data fitting with the Levich/Tafel/KL equation fitting. Both the SCM and conventional fittings were performed with a global charge transfer coefficient across all experiments. Summary of error metrics e) for both the classic planar SCM and the equation fitting for the experimental data indicating poor fits.

Figures 2c and 2d show the posterior distributions and extracted fit parameters for the exchange current density (j_0). These simulated distributions or extracted values for j_0 are plotted against total mass loading. There is a slight downward trend from

the SCM and a slight upward trend from the standard equations, but quantitative error metrics for both the SCM fitting and standard fitting show large RMSE and MAE across the experimental dataset shown in Figure 23. The magnitude of these errors undermine the credibility of any observed trends. Additionally, no clear trend exists with support ratio for either fit as observed in Figures 2c and 2d from the color legend for the support ratio.

The CV posterior predictions and equation fits across the experiments showed poor fitting in the mass transport limiting regime (see Figure S3 and S4). This indicates, unsurprisingly, that mass transport through the porous electrodes is not well captured in this set of physical equations (Levich, Butler-Volmer, and Koutecký-Levich). Although our classic planar SCM does incorporate electrode parameters along with these physical equations, there is no direct causal pathway connecting the support ratio or mass loadings to the limiting current, seen graphically in Figure 1. As such, we next investigated the validity of an SCM that includes directed edges connecting the electrode thickness to the limiting current density, which required modifications to the Levich equation.

2.2 Modeling mass-transport

2.2.1 Modified Levich Equation

To better model the effect of support ratio and total mass loading on mass transport, we constructed a variation of the classic planar SCM that includes both a causal pathway between electrode thickness and the limiting current density as well as a pathway between porosity and the limiting current density. The original Levich equation (Figure 3a) is first shown as follows:

$$j_{lim} \leftarrow 0.62nFD^{2/3}\omega^{1/2}\nu^{-1/6}C_b$$

Comparatively, the modified Levich equation (Figure 3b) is listed below:

$$j_{lim} \leftarrow nFC_b\left(\frac{1}{0.62D^{2/3}\omega^{1/2}\nu^{-1/6}} \times \frac{\delta_{tot}}{D_{electrode}}\right)^{-1}$$

where the $\frac{1}{0.62D^{2/3}\omega^{1/2}\nu^{-1/6}}$ term is the hydrodynamic coefficient, representing transport determined by the RDE rotation rate. The overall transport coefficient is the hydrodynamic coefficient modified by the transport through a porous diffusion layer (the porous electrode) above the catalytic surface through which the reactants (dissolved oxygen) must diffuse, see Figure 3b inset. We use $D_{electrode}$ for the diffusivity

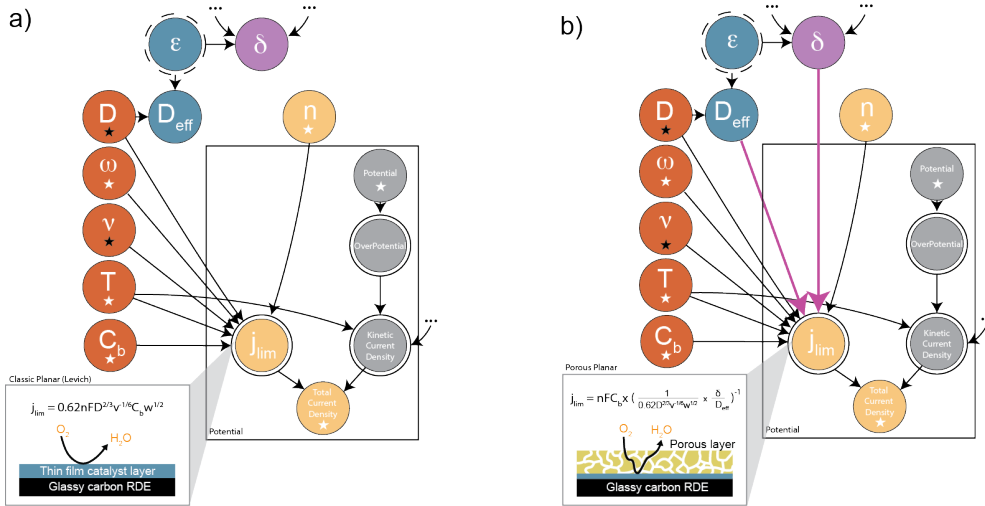


Fig. 3 A focused view of the a) classic planar and b) porous planar SCMs highlighting the limiting current density node and its parent nodes. The classic planar uses the Levich equation to model thin film catalyst layers (blue), whereas the porous planar model uses the modified Levich equation, where the reactants first diffuse through a porous layer (yellow) before reaching a catalytic surface. The equations are shown with the schematics.

of O_2 through the porous electrode (Bruggeman relationship: $(D \times \epsilon^{3/2})$, and δ_{tot} for the electrode thickness. This physical mechanism is similar to work by Knoche et al. [20]. We termed this model the porous planar SCM; the full page view is shown in Figure S5. The Butler-Volmer kinetic current equation and the K-L equation modeling the transition from kinetic to mass transport limited regimes remained the same. Figure S6 shows the simulated prior voltammograms from the porous planar SCM. After construction and prior assessment, the porous planar SCM was quantitatively validated as discussed in the next section.

2.3 Model Validation and Refinement: Prediction

Prediction and root-cause analysis using SCMs require different validation procedures. To assess predictive performance, clear separation between test sets and training is necessary, i.e., standard train-validation-test data split. (For root cause analysis discussed later, we no longer have ground truth and instead train on all available data.) Figure 4a shows the prior and posterior predictions for the porous planar SCM on the test dataset. Compared to the classic planar model, the porous planar SCM showed quantitative improvement across all evaluation metrics as summarized in Figure 4e. Metric details are described in the Methods [39–41]

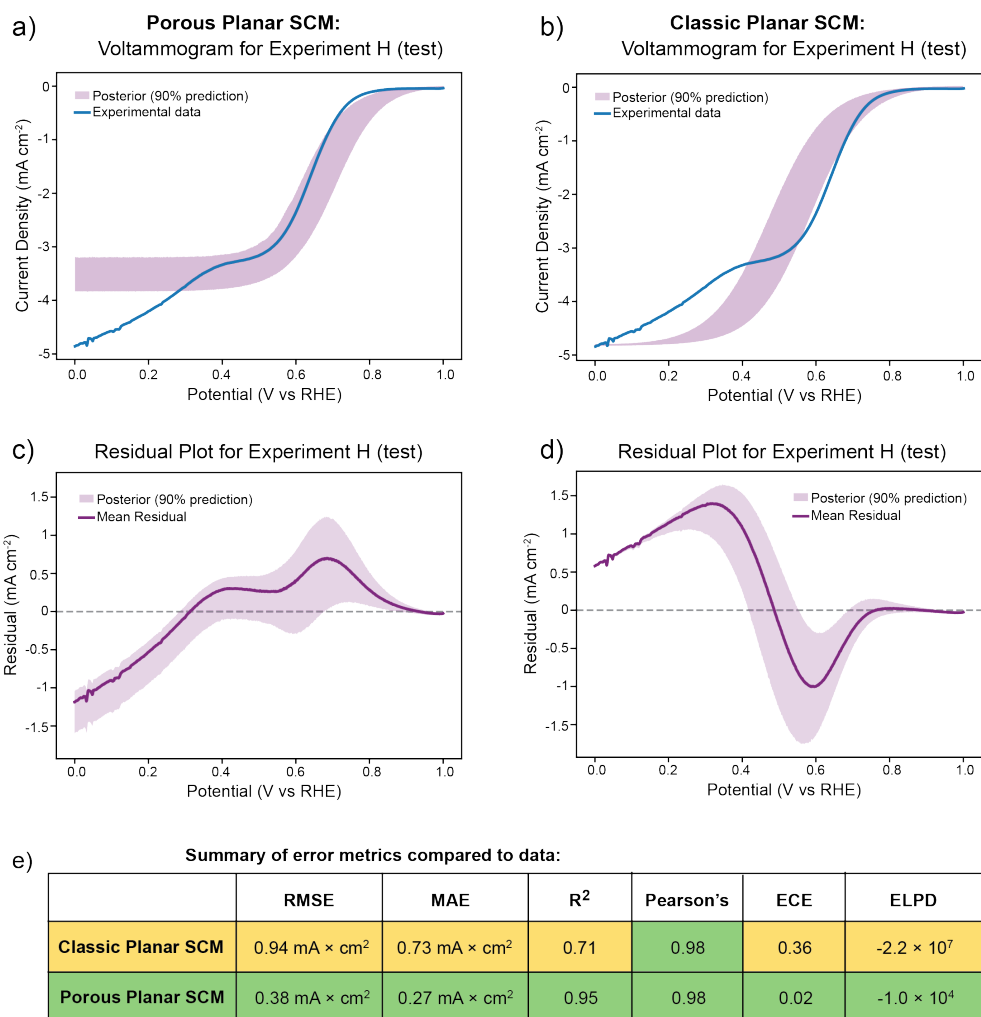


Fig. 4 Predictive performance of reverse sweep of oxygen reduction cyclic voltammogram of MnSb_2O_6 on Vulcan carbon using an RDE for (a) the porous planar SCM, and (b) the classic planar SCM, as evaluated on experiment H from the test set, and (c, d) shows residual plots for experiment H for the porous planar, and classic planar models respectively. The SCMs were trained on the combined training plus validation datasets. (e) Quantitative metrics comparing the predictive performance of the porous planar model and the classic planar models on the test set. The green highlight emphasizes the improvement in performance for the porous planar SCM compared to the classic planar SCM: smaller residual errors (RMSE and MAE), improved goodness of fit (R^2), and better calibration (Expected Calibration Error (ECE)) were observed. The Expected Log Predictive Density (ELPD) metric simultaneously evaluates the model's predictive accuracy and calibration on unseen data [41]: the less negative value for ELPD for porous planar indicates that unseen data is much more likely under the model.

There remains mismatch in the current density posterior prediction and the experimental data at the mass transport limited regime (Figure 4a,c), indicating further improvements to the porous planar SCM can be made. Figure S7 shows a summary “heatmap” pointing to specific nodes in the model with the most uncertainty. These include fraction active sites and utilization factor nodes. In essence, this highlights that the model relies on the uncertainty in these nodes to better fit the training data during training and give better predictions on the validation data. These nodes and their mechanisms are areas for model improvement. The ability to both update uncertainty distributions with respect to data and reason on the uncertainty is a major advantage enabled by the Bayesian probabilistic approach we used.

2.4 Manual Reasoning on the Porous Planar SCM Posteriors

While the model was critiqued on predictive performance (with regions identified for improvement), we also analyzed trends in the posterior distributions for the model trained on the entire dataset. Figure 5a shows the posterior prediction for experiment H when it was included in the model training. The porous planar SCM posteriors showed better fits to data compared to the classic planar SCM posteriors especially in the mass transport limited regime (Figure S8 and S3, both models trained on all data). Figure 5b shows the posterior distributions for exchange current density node, j_0 , for each experiment as a function of total loading and colored by support ratio. Rather than a single clear trend, the distributions suggest that even for the same total material loadings (e.g., experiments F, H, I), changing support ratio affects the j_0 . Analyzing the posterior distributions from the model trained on all data is similar to the earlier discussion comparing the classic planar SCM with the Levich/Tafel/K-L equation set shown in Figure 2. A direct fitting of the experimental data to the modified Levich/Tafel/K-L set of equations was also performed (Figure S9), however, the fit gave nonphysical thicknesses and unrealistic trends where the lowest loading experiment had the thickest electrode.

To investigate the root cause of support ratio and loadings on exchange current density, we plotted the posterior distributions of nodes causally upstream of j_0 , including N_{sites} and utilization factor nodes. From the posterior distributions in Figures 5d-f, any observable trends were still obscured. Therefore, while we began to investigate the effect of support ratio and material loading on catalyst performance by applying critical thinking on the trained model outputs, trends from this dataset remain challenging to disentangle when using conventional model analysis techniques. As such, we next focused on applying systematic and algorithmic causal reasoning on the SCM

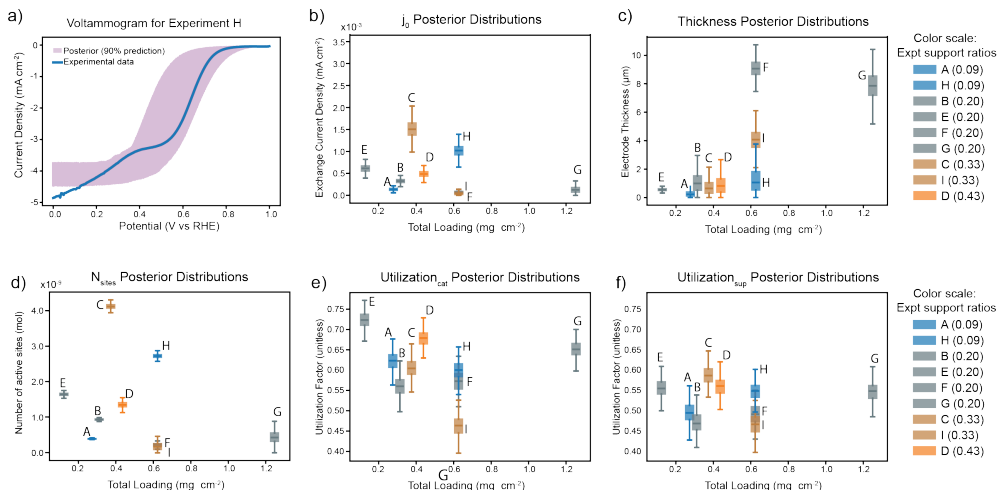


Fig. 5 Analyses of the insights from posterior distributions on the reverse sweep of oxygen reduction cyclic voltammogram of MnSb_2O_6 on Vulcan carbon using an RDE for the porous planar SCM trained on the entire experimental dataset; (a) The posterior prediction voltammogram for experiment H and (b-f) posterior distributions for the various experiments for each of the nodes exchange current density, electrode thickness, number of active sites, catalyst utilization factor, and support utilization factor. The per-node posterior distributions are plotted as a function of increasing total mass loading and colored according to the support ratio in each experiment.

and quantified the effects of support ratio and total loading through different causal pathways.

2.5 Decoupling support ratio and material loading using mediation analysis

Our findings from this section are two-fold: (1) the development of systematic and algorithmic causal reasoning methods for physics-based SCMs, and (2) the quantified answer to the question, *how does changing the catalyst-to-support ratio and the total material loading affect the total current density measured from voltammetry through a change in electrode thickness versus a change in the total number of active sites?* To ask the causal question and perform quantitative reasoning, we developed and applied dedicated software for querying SCMs (see [Causal Probabilistic Programming](#)) to the validated porous planar SCM. The scientific software tools we developed are published along with this manuscript ([Code availability](#))

The porous planar SCM contains two pathways where changing the support ratio or total mass can affect the total current density. The causal pathways are highlighted in Figure 6; the purple pathway indicates a mass transport cause-effect from changing electrode thickness, and the red pathway is a kinetic cause-effect from changing the

number of active sites. For instance, increasing the total mass loading can increase the total thickness of the electrode and further constrain the limiting current density; or increasing total mass loading can increase the number of active sites available and thus increase the exchange current density. Increasing the support ratio can also increase the thickness of the electrode (since the support is less dense than the catalyst).

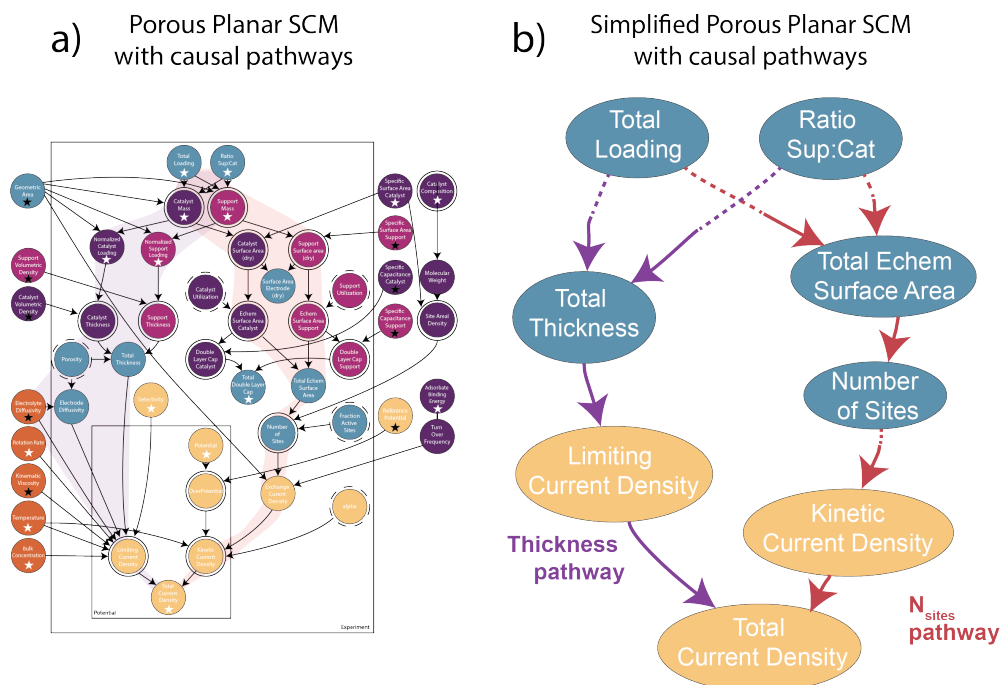


Fig. 6 Highlighted visualizations of the causal pathways in the porous planar model; (a) condensed view of the full porous planar SCM highlighted pathways with the purple highlight indicating the mass transport pathway via thickness, and red highlighting the kinetics pathway via number of sites and (b) a simplified view of the porous planar model with the key nodes for each pathway.

To interrogate the two causal pathways, the trained porous planar SCM was used to systematically simulate different “experiments” and quantitatively compare between them. First, we simulated a baseline experiment with support ratio of 0.09 and total loading of $0.27 \text{ mg}\cdot\text{cm}^{-2}$ (analogous to experiment A from Kreider et al., Table 1); the simulated voltammogram distribution is shown in blue in Figure 7a. We then simulated an experiment support ratio 0.54 and total loading of $0.5 \text{ mg}\cdot\text{cm}^{-2}$, shown in orange. The difference between the blue and the orange distributions is shown in Figure 7b.

Quantifying the difference between the blue baseline and the orange simulations caused by each of the causal pathways required additional simulations. In a third

simulation, we constrained the value for the N_{sites} to its value from the baseline experiment. This severs the causal pathway upstream of the N_{sites} (highlighted blue, Figure 7e) such that changing the support ratio and the total loading to the values in orange (support ratio 0.54 and total loading of $0.5 \text{ mg}\cdot\text{cm}^{-2}$) can *only* cause a change in the total current density through the thickness pathway (purple arrows). In causal reasoning terms, we instantiated a **counterfactual world**, in which we **intervened** on the total loading and support ratio *as well as the* N_{sites} . The counterfactual world of “effect through thickness only” is the instantiation shown in Figure 7e, and can be considered an “impossible control experiment”. The delta between total current density simulated from the counterfactual world in Figure 7e and the baseline experiment results in Figure 7c. Similarly, in a fourth simulation, we constrained the value for the thickness to its baseline value, i.e., the counterfactual world shown in Figure 7f, and the quantified “effect through N_{sites} only” is shown in Figure 7d.

The effect through thickness (Figure 7c) showed that increasing the support ratio to 0.54 and increasing the total loading $0.50 \text{ mg}\cdot\text{cm}^{-2}$ while keeping the N_{sites} at its value in the baseline caused a decrease in total current [magnitude]. Higher support ratios and loadings increased the thickness, causing a decreased limiting current value. In contrast, the effect through N_{sites} showed that increasing the support ratio to 0.54 and increasing the total loading $0.50 \text{ mg}\cdot\text{cm}^{-2}$ while keeping the thickness at its value in the baseline resulted in increased current density [magnitude] (Figure 7d). This procedure of comparing simulated, interventional control experiments is called **counterfactual reasoning**, and using counterfactual reasoning to quantify the path-specific effects is called **mediation analysis**.

The mediation analysis was systematically performed for 100 combinations of support ratio (0.1-0.9) and total loadings ($0.12\text{--}1.25 \text{ mg}\cdot\text{cm}^{-2}$) with reference to the baseline. The results of the 100 mediation analyses were compared at different potentials, as shown in the per-potential and per-effect heatmaps in Figure 8b-j, where each square in the grid is extracted from a separate set of the simulations discussed in the previous paragraphs. We emphasize here again that the results from the mediation analysis are a demonstration of this new methodology to deconvolute coupled effects such as increased N_{sites} and thickness from increasing support ratios and total material loadings. The development of the porous planar SCM and application of probabilistic programming (see [Causal Probabilistic Programming](#)) enabled this preliminary effort into root cause analysis in electrochemical devices.

To discuss the results in detail, we first look at the 0.73 V heatmap for total effect (Figure 8b). The pink highlighted square indicates the total effect on current

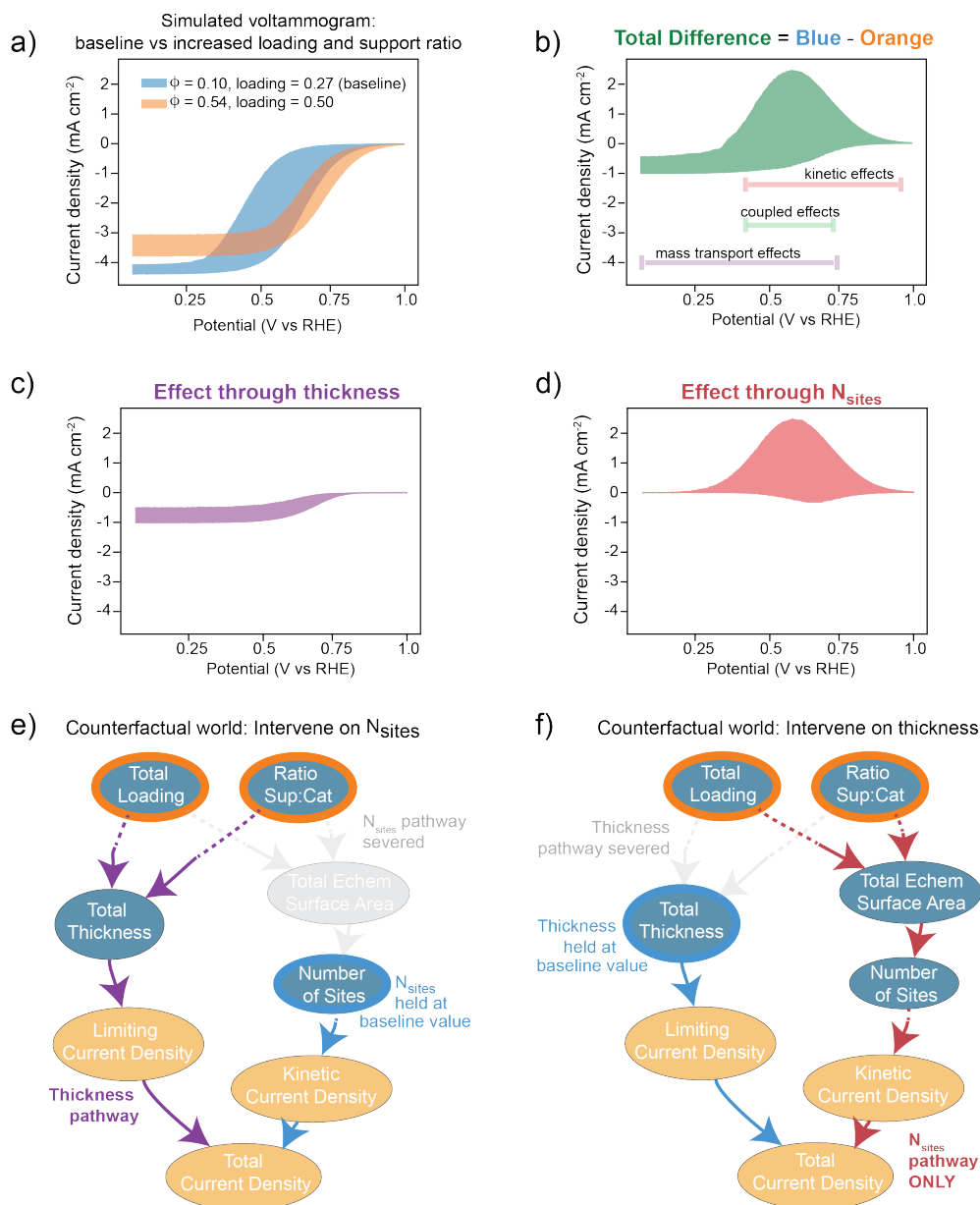


Fig. 7 Mediation analysis results of oxygen reduction cyclic voltammogram of MnSb_2O_6 on Vulcan carbon using an RDE with (a) the simulated voltammograms for the blue baseline experiment (support ratio = 0.10, total loading = $0.27 \text{ mg}\cdot\text{cm}^{-2}$) and orange new experiment (support ratio = 0.54, total loading = $0.50 \text{ mg}\cdot\text{cm}^{-2}$), (b) the difference between the blue and orange, (c) the effect of changing the support ratio and total loading through the electrode thickness pathway only showing decrease in performance (negative effect a.k.a. decreased current density magnitude) and (d) the effect of changing the support ratio and total loading through the N_{sites} pathway only showing an increase in performance (positive effect a.k.a. increased current density magnitude). The counterfactual instantiations that enabled the isolated effect through each pathway are shown in (e) and (f), respectively, and can be considered “impossible control experiments” as enabled by our model and methods development.

density caused by increasing the support ratio to 0.54 and total loading to $0.5 \text{ mg}\cdot\text{cm}^{-2}$ compared to the baseline experiment (dotted black square, support ratio = 0.10 and total loading = $0.27 \text{ mg}\cdot\text{cm}^{-2}$). A positive current effect at the pink square is observed, as emphasized by the blue color scale, i.e., the current density magnitude increased at 0.73 V, corresponding to increased performance. We note three main trends in Figure 8b when changing support ratio and total loading: starting at the baseline dotted black square and following the black dotted arrows, we observe (1) negligible changes, (2) monotonic increase, or (3) non-monotonic changes in total current. The non-monotonic trend indicates convoluted causes that we begin to disentangle using the mediated effect results from the two causal pathways, N_{sites} and thickness.

The quantified effect through thickness and effect through N_{sites} at 0.73 V heatmaps are plotted in Figures 8c and 8d, respectively. A monotonic increase in performance is observed when increasing to high ratios and loadings via the thickness pathway (Figure 8c, dotted arrow (2)). This trend indicates that at high support ratios and loadings, thick electrodes will decrease catalytic performance when number of sites is held at baseline. Intuitively, this aligns with the non-monotonic change in the total effect, Figure 8b dotted arrow (3), to indicate a trade-off between more material (more active sites) with thicker electrodes (decreased transport). The mediated effect through thickness decouples part of the non-monotonic trend observed in the total effect.

In contrast, the effect through N_{sites} at 0.73 V, Figure 8d, shows a monotonic increase in performance is observed when increasing from the baseline to moderately low total loadings and high support ratios via the N_{sites} pathway (dotted arrow (2)) but a non-monotonic increase is observed when increasing to high support ratios and high loadings, (dotted arrow (3)). This means that high loadings and high support ratios beyond ~ 0.54 do not increase N_{sites} as much as increasing to moderate loadings with moderate support ratios when thickness is held at the baseline value. There may be an optimization of N_{sites} when changing support ratio and total loading that is *independent* of the electrode thickness effect; see [Discussion](#).

Next, looking at the total effect heatmap for 0.59 V, Figure 8e, we observed similar convoluted non-monotonic trends. Since the 0.59 V is around the kinetic/mass transport regime transition, the effects of both thickness and N_{sites} are more pronounced than at 0.73 V. For the heatmaps at 0.32 V (Figure 8h-j), which is strongly in the mass transport limited regime, only a decrease in performance due to increased electrode

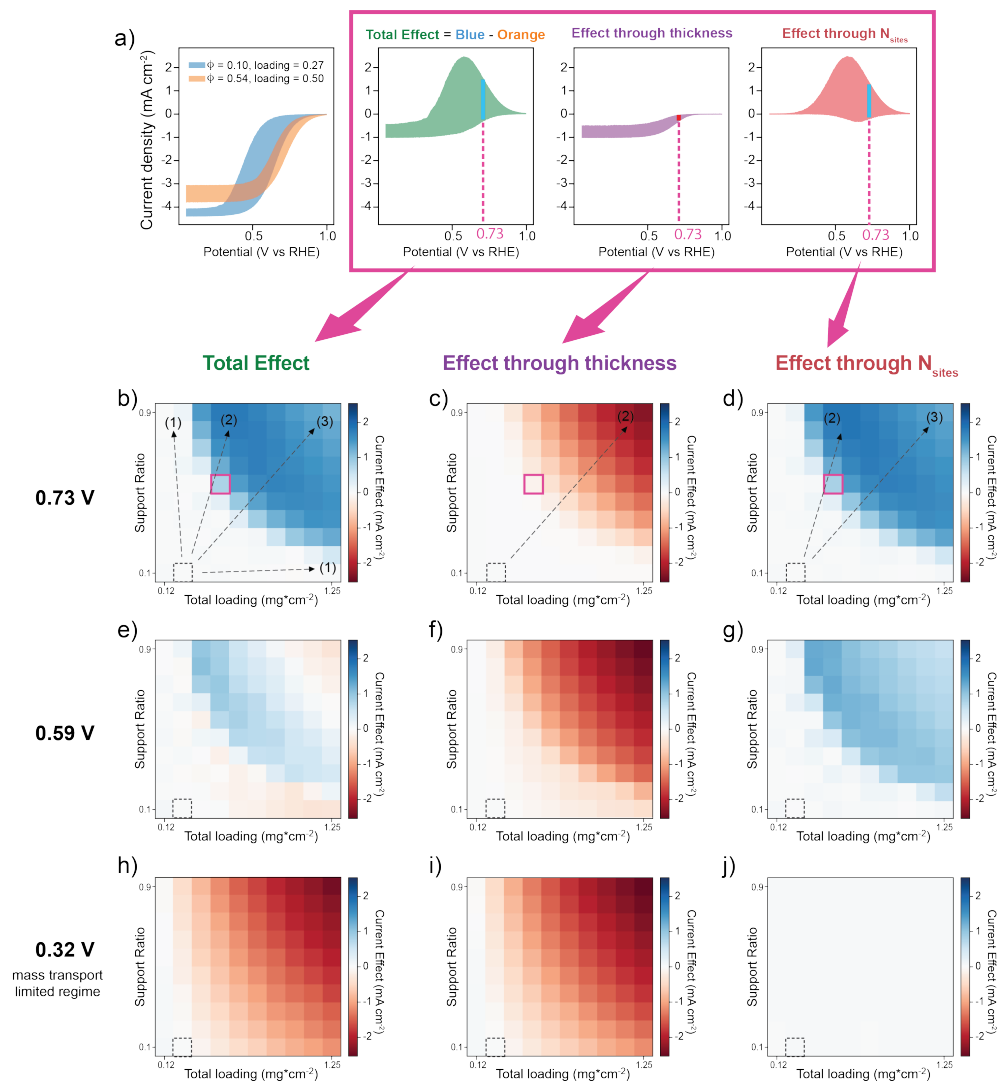


Fig. 8 Heatmaps showing the systematic mediation analyses comparing simulated experiments for 100 combinations of support ratio (0.1-0.9) and total loadings ($0.12-1.25\text{mg}\cdot\text{cm}^{-2}$) with reference to the baseline support ratio = 0.10, total loading = $0.27\text{mg}\cdot\text{cm}^{-2}$. Each square in the grid represents the results at a specific potential for a single mediation analysis as explained in Figure 7 and depicted again in (a). A heatmap is generated per-potential and for the (b,e,h) total effect, (c,f,i) effect through N_{sites} via the counterfactual world in Figure 7e, and (d,g,j) effect through thickness via the counterfactual world in Figure 7f. The black dotted square highlights the baseline experiment. The color scale indicates a positive effect on current density magnitude (increased performance) with blue shades and a negative effect on current density (decreased performance) with red shades. The pink square highlights the effects at 0.73 V for the support ratio = 0.54 and total loading = $0.5\text{mg}\cdot\text{cm}^{-2}$ example, corresponding to the pink dashed lines in (a). The black arrows indicates different trends observed compared to the baseline experiment: 1) no trend, 2) monotonic increase or decrease, and 3) non-monotonic behavior. All potentials referenced to RHE. We also emphasize the method development enabling the application of SCMs and causal reasoning to this electrocatalyst system shown in this figure as part of our results.

thickness is observed. Together, the heatmaps in Figure 8 emphasize the thickness- N_{sites} trade-off on performance and also point to the additional convoluted trends in N_{sites} caused by support ratios/total loadings.

The mediation analysis with the porous planar SCM reveals the observed causes only after training on the experimental data. In other words, these simulations from the trained model reflect what can be learned from the experimental dataset. Notably, the heatmaps from an untrained model (Figure S10) only show the trend of poor mass transport at mass transport limited regimes. Figure S11 shows the same set of heatmaps but referencing different experiment baselines. Similar trends are observed that also highlight the trade-offs between decreased mass transport through electrode thickness and increased kinetics through N_{sites} when at high loadings and support ratios as well as the possibility of some N_{sites} optimization. Maximizing the insights from the SCMs therefore requires understanding the experimental data and questions, building a representative model, and training the model; this led to the development of a proposed workflow we discuss in the next section.

2.6 Structural Causal Modeling Workflow

To the best of our knowledge, this work presents the first application of structural causal modeling to electrochemical devices. Furthermore, our SCM causally connects root material properties to physics-based models. Given the complexity in modeling electrochemical systems, we present our model building workflow shown in Figure 9 as an important outcome that underscores the utility, interpretability, and credibility of the structural causal modeling framework. This workflow development was inspired by Bayesian inference workflows and causal modeling with real world data in other applications, specifically discussions on model iteration and inclusion of domain expertise [42, 43].

First, the system and causal questions are defined; we advocate for early inclusion of and reference to experimental datasets while constructing models in order to increase the transferability of modeling results. During the model building steps, initial model critique and evaluation is done via prior predictive checks. The model is then trained on the experimental data. Model performance in the mediation analysis is both qualitatively and quantitatively assessed to identify major modifications (as indicated by the loop back to “build full SCM” step). Separately, the model is assessed through a validation loop, whereby the train-validation-test data split is used to quantitatively assess model predictions and iteratively tune hyperparameters (kernel widths). From this workflow, the root-cause analyses performed with the prediction-validated model

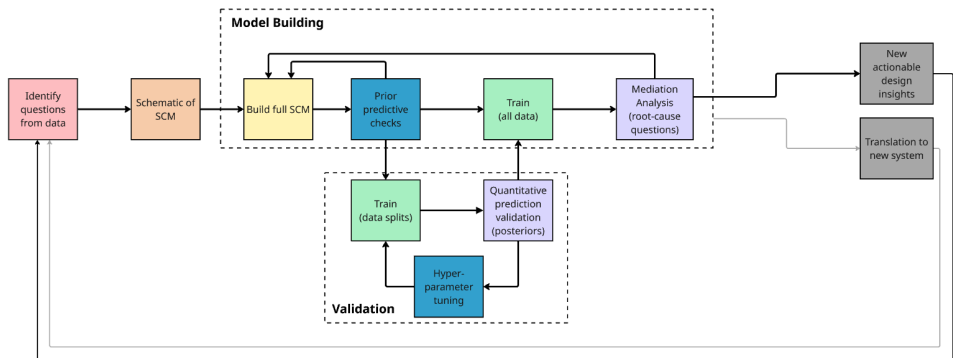


Fig. 9 Causal modeling workflow summary. The workflow begins with identifying the questions with respect to an experimental dataset (or for future applications, defining an experimental dataset for the causal model from identified causal questions), then constructing the SCM, validation and training, then causal reasoning such as using mediation analyses. The final steps in the workflow are identifying actionable design insights from the model and analyses as well as translating similar models/questions/analyses to new systems. Both of the final steps loop back to the identification of questions and experimental data, with the goal of improving the translation of experimental and fundamental studies to breakthrough materials/device designs

enables deeper understanding of the experimental dataset and poses new hypotheses or actionable design insights. We present this workflow as a method for discovering new research directions in this field as well as related electrochemical systems including, but not limited to, various devices and device scales within the electrolyzer, fuel cell, and battery communities.

3 Discussion

To summarize, we developed a structural causal model with the capability for systematic causal reasoning on how support ratio and mass loadings affect catalyst performance in an RDE experiment. This work demonstrates the first application of structural causal modeling with physics-based equations to materials science. The SCMs we developed are trained on experimental data, analogous to machine learning models. An important point to note is that, contrary to popular machine learning methods such as neural networks, our SCMs models are compatible with small datasets. The incorporation of well-known equations from the field of catalysis along with causal relationships connecting electrode and material properties into our SCMs mitigates the necessity for large datasets. These equations and relationships serve as the strong inductive bias that enables the use of small datasets (as opposed to data-driven ML methods that search for patterns without built-in constraints) and also requires little

compute power (Figure S12 and [Code availability](#)). Furthermore, the graphical representation of SCMs enables clear interpretability and explainability of the model, akin to functional block diagrams used in engineering [44, 45]. We emphasize that the classic planar SCM is the augmentation of conventional physical equations with causality and probability that enable use of novel causal inference tools.

As such, it is extremely important to validate our models’ predictive performance. Errors in the assumptions will lead to under performance. This was observed when the porous planar SCM quantitatively out-performed the classic planar SCM precisely, because the assumptions of a planar non-porous electrode did not hold given the experimental data. We used the quantitative metrics and the validation workflow presented to support the applicability of the porous planar SCM, outline standard operating procedures for validating SCMs, and also specifically indicate areas for model improvement. Although the porous planar SCM used in the mediation analyses can be further improved, this work is focused on the *development of new methods and tools (of which model critique is included)*. The use of SCMs and causal reasoning with experimental datasets can accelerate understanding of material performance as well as new hypotheses evaluation and generation. Specific in this demonstration, the models and methods present new insights into the ORR catalyst system with entangled root causes.

We identified two key insights from the mediation analyses with the porous planar SCM. The first is the general impact of electrode thickness, whereby increasing support ratio and total material loading causes changes to the electrode thickness that can decrease catalyst performance particularly at the mass transport limiting regime. While this result is not ground-breaking [17, 46, 47], we disentangled and quantified the mass transport and kinetic effects at different operating potentials in the RDE experiment as well as identified regimes (the combination of support ratios, total loadings, and operating potentials) where there is trade-off between thicker electrodes and increased N_{sites} . The decoupled quantification is enabled by the “impossible control experiments” in the counterfactual reasoning, which requires the development and application of our SCMs. These model results highlight the need for additional experimental studies with a focus on tailoring or quantifying the electrode thickness. This could include adding electrode thickness measurements to the experimental workflow, such as atomic force microscopy on drop-cast electrodes, and or changing solvent ratios in the ink formulation to impact the morphology of drop-cast electrodes.

The second key insight from the mediation analyses is the identification of additional convolution between the support ratio and total loading on the N_{sites}

even when the electrode thickness is held the same. This is suggestive of differences in utilization factors, for instance due to differences in agglomeration at different support ratios or porosity effects on utilization factors. Experiments to control the N_{sites} may be challenging to design and verify, but could include changing catalyst particle size while using the same loadings and aiming to control thicknesses (catalyst active surface area and therefore N_{sites} can change). The entangled variation of N_{sites} with support ratio and thickness result also aligns with the highlighted areas for model improvement (shown in Figure S6), where uncertainties remain with the utilization factors. Furthermore, there may be additional causal relationships to add between the support ratio and utilization factors.

We propose a few improvements to the model relevant to the insights from the causal analyses. However, we assert that such model improvements are beyond the scope of this work, which focuses on the development of new causal reasoning tools and methods using the classic planar and porous planar SCMs as baseline examples and first time presentations of the SCM framework. First, additional causal mechanisms are needed between support ratio and utilization factors as well as conductivity and electrode porosity. Ionomer content is also not currently modeled [48–52]. Next, selectivity (especially for these catalysts) is an active research area, therefore modeling the selectivity needs further refinement. The activity of the Vulcan carbon support may also require additional nodes that allow future mediation analyses into understanding support optimization. Finally, careful concentration modeling via the use of differential equations such as Fick’s 2nd law with reaction sink terms and concentration dependent Butler-Volmer equation requires major upgrades to our software development. Further details on suggested improvements can be found in the SI. As the first application of SCMs to materials electrochemistry, this work has resulted in new physical SCMs and insights, as well as a proposed workflow for decoupling convoluted ink parameters of which suggested model improvements are a part.

4 Conclusion

Detailed understanding of the electrode as a sum of its parts is necessary to understand complex coupled phenomena as well as translate RDE experiments to predict catalyst performance in electrode assemblies and large stacked electrode devices. SCMs are a modeling framework that enables new reasoning capabilities and insights into disentangling related experimental parameters and material properties. We constructed the porous planar SCM and quantified the effect of changing support ratio and total

loading on electrocatalytic performance through two different causal pathways: a electrode thickness path and a number of active sites path. We highlighted the trade off between increasing the number of active sites and increasing thickness as having opposing effects on total current density. Using the unique causal reasoning tools of counterfactuals and interventions, we also identified an additional coupled phenomena for optimizing the number of active sites through adjusting support ratio and total loading, even when constraining the electrode thickness. We apply this finding to suggest additional experiments and modeling directions.

While the SCMs presented in this work were constructed with a specific experimental dataset in mind, we believe in the generalizability of these models and workflow to other electrochemical systems. The construction of the models, development and application of methods, and analysis of insights presented in this work required a multi-disciplinary approach, combining material science and engineering, electrocatalysis, mathematical modeling, statistics, and computer science/machine learning expertise. Furthermore, the integration of physical equations into SCMs enables the application of machine-learning-like training methods and systematic causal reasoning to small experimental datasets. Leveraging this new multi-disciplinary and accessible framework, we advocate for SCMs as a useful quantitative and visual tool in bridging material innovation and research to device performance and deployment.

5 Methods

5.1 Experimental Details (from Kreider et al.)

In this work, the experimental data for training the models were sourced from published work by Kreider et al. [15]. The catalyst synthesis details, electrode fabrication methods, RDE set-up, and computational details are briefly summarized here: Colloidally synthesized MnSb_2O_6 nanoparticulate catalysts were primarily a mix of trigonal and rutile phases with small Mn_2O_3 impurities as seen by x-ray diffraction. Mn and Sb ratios were quantified by x-ray photoelectron spectroscopy. Ex-situ surface area was measured using Brunauer-Emmett-Teller (BET) isotherm analysis of N_2 physisorption. Inks were made by mixing pre-determined amounts of as-synthesized MnSb_2O_6 catalysts with commercial vulcan carbon in isopropyl alcohol and Nafion. Electrodes were made drop-casting inks onto RDEs. For electrochemical analysis the RDE used a polished exchangeable glassy carbon disc electrode (0.196 cm^2). Selectivity was measured on a representative sample using a Au ring disc electrode and

maximum H_2O_2 selectivity was used for training across all potentials. All electrochemical measurements were taken in 0.1 M KOH with a Ag/AgCl reference electrode with 85% iR correction. All potentials were shifted to a reversible hydrogen electrode (RHE). CVs were done in O_2 saturated electrolyte at 1600 rpm. O_2 -saturated CVs were corrected by subtraction of CVs in N_2 -saturated electrolyte and only the forward or reverse scan was used for training (based on which was taken first). Double layer capacitance measurements were measured of the entire electrode at 0.5 V vs RHE from CVs at multiple scan rates in N_2 -saturated electrolyte. DFT OH-adsorption was based on the 001 surface.

5.2 Structural Causal Models

The models we explore in this paper can be described mathematically as **Structural Causal Models (SCMs)**, which has been developed within the computer science and statistics research communities over the past several decades. Informally, SCMs are defined as a collection of deterministic functions known as **structural functions** of the form $Y \leftarrow f(\text{Pa}(Y), \epsilon y)$, where $\text{Pa}(Y)$ represents the parents of Y in a corresponding causal graphical model and ϵy is an exogenous noise term. Note the use of an arrow, “ \leftarrow ”, rather than an equals sign, “ $=$ ”. The arrow indicates that changes in the right-hand-side of the expression cause changes in the left-hand-side, but not vice versa. For a formal mathematical definition, see Pearl 2009 [29].

A fully specified SCM enables the use of many low-level probabilistic modeling operations that can be composed to answer high-level analytical questions. What makes SCMs mathematically distinct from other probabilistic models is their support for two causal-specific mathematical operations: **intervention** and counterfactual world-splitting. Interventions represent a hypothetical (and potentially impossible) control experiment in which a variable’s value is assigned according to a user-specified value or function, and all other variables are left unchanged. This is formally modeled by producing a new SCM in which the intervened variable’s structural function $Y \leftarrow f(\text{Pa}(Y), \epsilon y)$ is replaced with the structural function $Y \leftarrow y'$, where y' is the intervention assignment. Counterfactual world-splitting represents the process of imagining an alternative world, and is formally modeled by duplicating all variables and structural functions in an SCM then intervening on one or more variables. In isolation, counterfactual world-splitting provides little of value. However, when combined with interventions these counterfactual world-splitting operations can be used to formally represent rich causal questions. For example, questions about mediation analysis can be formally represented mathematically by first instantiating parallel counterfactual

worlds, and then intervening on the value of mediators in one world to be the same as value in another world. For a detailed discussion, see work from Pearl [53].

Furthermore, we use an extension to SCMs known as Bayesian Structural Causal Models (BSCMs) [37]. Using BSCMs, modelers posit (potentially hierarchical) distributions over structural functions themselves, as well on the exogenous noise terms as in ordinary SCMs. In this way, “learning” structural causal models from data is reduced to joint probabilistic inference as in ordinary Bayesian statistical methods a la Bayes rule, and often approximated using approximation algorithms. This provides a principled framework for representing broad uncertainty, to reason about how that uncertainty is updated in light of data, and how that uncertainty propagates to the causal questions that are often of interest in scientific domains.

5.2.1 Translating experimental workflows and physical equations into SCMs

In this work, we translated conventional physical equations into SCMs, whereby the structure (e.g. edges connecting nodes) encodes causality. Specifically, the directionality of the edges in the causal graphical model representations (e.g., Figure 1) stipulate a cause going to an effect. This directionality necessitates that changing a “cause” will impact an “effect”. For instance, the Butler-Volmer equation is translated into a causal relationship in which an applied overpotential *causes* a change in the total current density. The directionality preserves the interpretability of the physics in the SCM during model simulations and data fitting. Specifically, for the RDE experiments modeled in this work, overpotential is the experimental control being directly applied, therefore we construct this directed causal relation. We note that this can be a different approach to modeling and fitting compared to conventional equation fitting: the Butler-Volmer equation (Tafel approximation) is often rearranged so that $\eta = (slope) \times \log_{10}(i/i_0)$, however, in this rearrangement, current density or exchange current density do not cause overpotential. For the conversion relationships used in this model (e.g., catalyst mass [mg]/geometric area [cm²] \rightarrow catalyst mass loading [mg*cm⁻²]), we ascribed a causal direction to match an “experimental workflow”: a target total material loading and support ratio is selected by the experimentalist \rightarrow individual amounts of catalyst and support are calculated (and weighed out) \rightarrow the catalyst and support loadings are calculated from the electrode geometric area. We note that causality in these conversion relationships may appear contrived, however they enable the unique causal questions with intervention handles shown in this work. Future work aims to address the equivalency of these conversion relationships.

Another structural element in the SCM is the hierarchical organization of repeated structures in the causal model into **plates**. Essentially, this captures the multiple individual experiments and measurements performed in an experimental dataset, where the support ratios and the total material mass loadings were changed, and for each experiment, a cyclic voltammogram was measured. While the support ratios and the total mass loadings in the different experiments may differ, the causal relationships between mass, surface area, thickness, etc. are the same across the experiments (these are repeated structures). The first plate in our SCM is the experiment plate to represent all experiments across a set. Similarly, while the applied potential is different for each data point in the cyclic voltammetry measurement, which consists of many potential-current data points, the way applied potential affects overpotential, kinetic current density, etc. remains the same across the timepoints. For ‘n’ number of experiments we model, there will be ‘n’ experiment plates, and for ‘x’ number of data points in the cyclic voltammogram, there will be ‘x’ number of potential plates. This hierarchical plating structure is shown in Figure 1b via the boxes framing nodes that are in the experiment plate and the nested potential plate.

The third important element of our physics-based SCMs to note is specification of uncertainty. As mentioned, the mathematical structural functions in SCMs include exogenous noise terms. In our physics-based materials-device SCMs, we apply the noise terms as probability distributions that represent uncertainty stemming from measurement errors and uncertainty in the mechanisms or values (epistemic uncertainty). An example of uncertainty in the measurement is the Gaussian distribution we applied to the total current node to represent instrument error ($\sim 0.01 \text{ mA/cm}^2$). An example of uncertainty in the values may be seen in the porosity node. Porosity is challenging to measure/not measured in the experimental dataset, therefore we give the porosity root node an initial value of 0.5 with a beta probability “kernel”. The **kernel** is a functional which accepts parameters as inputs and returns distributions. This is effectively stating that our initial belief about porosity, is some value centered around 0.5, but may be slightly larger or smaller. This also means that if the model is used to run many simulations, with each simulation sampling from the porosity prior distribution, all downstream nodes will necessarily also be a distribution rather than single scalars. An example of uncertainty in the mechanisms can be demonstrated with the total ECSA node. Total ECSA is caused by the ECSA_{cat} and ECSA_{sup} : if the catalyst had an ECSA of 20 cm^2 while the support had an ECSA of 15 cm^2 , then the total electrode would have an ECSA of 35 cm^2 . This value would then be combined with a Gaussian kernel to generate a Gaussian distribution centered at 35 cm^2 . This distribution would

then be used to represent both the value and uncertainty of our estimates for ECSA. Note that the applied Gaussian distribution to the Total ECSA is added in addition to the distribution of values caused by the incoming nodes, which are also distributions. Additionally, specific to the prior generation, we applied uniform kernels to several of the nodes that we intended to sweep. For instance, the applied voltage node was ascribed a uniform kernel centered at 0.6 V with lower bound 0 V, and upper bound of 1.2 V. This allowed the generation of the voltammogram prior distributions.

We also further describe our entire model building process here: given the small dataset and the pioneering physics-based model this work presents, initial model construction and performance was done while training on the entire dataset. The model performance was evaluated on mediation results and alignment with experimental intuition and hypotheses. This was done to investigate mass transport modeling in porous electrodes. The modified Levich mechanism in the porous planar model was initially assessed on the mediation results on mass transport effects and trained with the entire dataset. Further major adjustments to the model such as the addition of porosity and plating structure were also done with respect to mediation performance. Once the main structure of the model had been sufficiently established, small adjustments and refinements to the model were done based on the predictive performance, which required a train/validation/test data split. See the [Data hold-outs](#) for clear listing of the data splitting in different parts of the workflow.

5.3 Model Training

We used stochastic variational inference (SVI) to approximate the posterior distributions over SCM model parameters, which propagate to uncertainty estimates over causal effect estimates [54]. SVI algorithms involve first defining a variational family over a collection of random variables X and parameterized by ϕ , denoted $Q(X; \phi)$. For example, Q could be a collection of Gaussian random variables where ϕ represents the mean and variance of each Gaussian distribution. To approximate a posterior distribution, SVI involves optimizing ϕ to minimize an upper bound on the Kullback-Leibler divergence between Q and the (unknown) posterior distribution $P(X|Data)$, a quantity known as the evidence lower-bound (ELBO). Even though the true posterior distribution $P(X|Data)$ is unknown, SVI algorithms can still optimize ϕ by computing stochastic estimates of the gradient of the ELBO from available numerical quantities, and then using those stochastic gradients in an iterative gradient descent algorithm. This procedure effectively reduces probabilistic inference, which involves

solving an intractable integral, into a numerical optimization procedure that can be scaled to hundreds of thousands of parameters and data points.

The kernels described earlier also serve as ways to add domain knowledge and subject matter expertise to SCMs and can affect model training. For example, if we are certain that the total electrode loading is a sum of the support loading and catalyst loading, then the kernel we apply to total electrode loading should have a narrow standard deviation. This leads to narrow prior distributions for total electrode loading. Narrow kernels incentivize model training to stay near the initial guesses, while wide kernels allow model training to diverge from initial guesses, where “initial guesses” for variables comprise both the kernel and the structural equation for the variable. This idea of implicit incentivization is referred to as “regularization” in optimization and machine learning communities. Thus the kernels we choose are model regularizers.

We used a clipped Adam optimizer, with a 5×10^4 learning rate, no learning rate decay, and 4,000 training steps.

5.3.1 Data hold-outs

Different data hold-out strategies were utilized during the modeling process. For the initial modeling building, all data used for training and evaluated on mediation results, see model building section above. For fine-tuning and model refinement, the model was trained on the training set ($n = 6$), then quantitatively assessed on the validation set ($n = 2$). Small adjustments to the model (initial default values, uncertainty parameters) were made and the training/validation loop was repeated. After this iterative refinement, the model was assessed for its predictive performance on the test set: the model was trained on the combined training and validation set ($n = 8$) and quantitatively assessed on the test set ($n = 1$). Lastly, the mediation analysis for new insights utilized the model trained on the entire dataset.

5.4 Causal Probabilistic Programming

Causal probabilistic programs automate many of the symbolic and numerical operations used in probabilistic and causal modeling and reasoning, including interventions, counterfactual world-splitting, probabilistic sampling, probabilistic density function evaluation, and many more. These systems build on existing software systems for differentiable tensor computations, which have been developed extensively for machine learning workflows. We use ChiRho [55], a causal probabilistic programming language built on the Pyro probabilistic programming language [56] and the PyTorch tensor computation system [57]. These systems automatically translate causal models and

causal questions into numerical operations that themselves can be automated using automatic differentiation [58] and compiled to massively parallel GPU hardware. See Figure S11 for a schematic diagram of causal probabilistic programming systems.

5.5 Validation

We supplemented our model quality assessment with quantitative metrics. The metrics include (1) the accuracy of the predictions, (2) the quality of the predictions’ uncertainties [39], and (3) the goodness-of-fit, which is whether the model’s errors show leftover patterns [40]. We assess model prediction accuracy using Mean Absolute Error (MAE), Root Mean Squared Error (RMSE), and coefficient of determination (R^2). MAE weights all errors equally and is common in the machine learning community, while RMSE disproportionately punishes outliers and is common in the statistics community. R^2 measures how much of the spread in the data can be explained by the model’s predictions. It ranges from 0–1, where 0 corresponds to a model that simply guesses the average and 1 corresponds to a perfect model.

We assess model uncertainty using Expected Calibration Error (ECE). The probability distributions from our models are used to create prediction intervals and assessed on their confidence. For example, an 80% prediction interval is the middle 80% of the simulated distribution—the 10th to 90th percentiles. A calibrated model means that an 80% prediction interval contains roughly 80% of the data. ECE measures the difference between our prediction intervals and reality. A higher ECE indicates the model reports more confidence despite being less accurate and is shown mathematically below:

$$ECE = \sum_{m=1}^M w_m |p_m - \hat{p}_m|$$

where M = number of prediction interval levels we evaluate (we used 0.01, 0.02, . . . 0.99); p_m = the width of the prediction interval level (e.g., 0.8 for an 80% prediction interval); \hat{p}_m = the fraction of observed values that actually fell within the model’s p_m prediction interval; and w_m = weight for interval m . This weight can be modified in general, but we used a uniform weight of 1 for all values of m .

We also assess model accuracy and uncertainty simultaneously using Expected Log Predictive Density (ELPD). ELPD evaluates where the actual data point falls on the predicted distribution and records the probability the model assigned there. High probability at the true value indicates the model anticipated the outcome well; low probability indicates it was surprised. ELPD combines these probabilities across all data points and rewards models that consistently place high probability on what actually occurred. High values of ELPD are better — e.g., -50 is better than -200.

Lastly, we assess model goodness-of-fit (i.e., whether the model’s residuals have patterns) using Pearson’s correlation coefficient (r), residual diagnostics, and posterior predictive checks. Pearson’s correlation coefficient (r) measures whether the model’s residuals follow a straight-line pattern when predictions are plotted against observations; it ranges from -1 to 1, with 1 corresponding to a perfect fit.

5.6 Glossary of terms

- **Structural Causal Model:** mathematical modeling framework which includes cause-and-effect relationships between variables. The relationships are modeled by structural functions, meaning that changing input causes influences output effects, but changing output effects does not influence input causes. SCMs can be represented in a causal graph, specifically a directed acyclic graph in which there are no loops.
- **Node:** the variables in the structural causal models. Root nodes have no upstream causes.
- **Edge:** the causal relationship between nodes. Graphically represented by directional arrows connecting nodes
- **Mechanism** or **Structural Function:** mathematical functions that describe a node as a function of its direct causes. An example for the structural function $f(a, b) \rightarrow c$ could be $a \times b \rightarrow c$.
- **Kernel:** functionals that intake parameter values and return distributions. We specify and use several types of distributions such as normal, folded normal, beta, etc.
- **Plate:** structural elements of the SCM that denote repeating independent units, such as different experimental samples. Graphically represented as boundary boxes that group the repeated nodes.
- **Prior distribution:** simulated distributions (for the nodes in the model) before training the model on data.
- **Training:** the model is conditioned on data and approximate posterior distributions are updated in order to better reflect the data. In this work, stochastic variational inference was used during model training.
- **Posterior distribution:** simulated distributions after the training
- **Intervention:** deliberate constraining or setting a variable to (e.g., different from its natural value). Also known as a ”do-operator” in the causal research community.

- **Counterfactual reasoning:** comparing “what if” interventions. In the SCM framework, evaluating the different outcomes when different node values are artificially constrained/set.
- **Inference:** In the context of Bayesian modeling, inference is the process of estimating approximate posterior distributions conditioned on data. This should not be confused with inference in the broader machine learning and neural network research communities, where inference is the calculation of graph outputs given graph inputs.

6 Acknowledgments

Our paper used previously data from Dr. Melissa Kreider. We appreciate that her work was easily accessible and formatted in a manner that was easy to use. We also appreciate Dr. Kreider’s thoughtful comments that helped us refine this work. We thank our co-workers at TRI for insightful conversations, specifically Dr. Steven Torrisi, Dr. Rumen Iliev, Dr. Joeseeph Montoya, and Dr. Brian Storey.

7 Author contributions

E.W., L.H., S.W., M.B.S., and K.T. jointly conceived the project, developed the structural causal model, interpreted the results, and wrote and edited the manuscript. E.W. led the writing efforts. S.W. and K.T. co-led the causal modeling software and computational development and M.B.S. and E.W. co-led the electrocatalysis experimental and material physics integration efforts.

8 Competing Interests

The authors declare no competing interests.

9 Data availability

Source data are provided with this paper. See GitHub repositories below.

10 Code availability

The code used to perform this work is available at: <https://github.com/TRI-AMDD/Whyzen-Public> and <https://github.com/TRI-AMDD/Whyzen-RDE-Public>

References

- [1] Shinozaki, K., Zack, J. W., Pylypenko, S., Pivovar, B. S. & Kocha, S. S. Oxygen reduction reaction measurements on platinum electrocatalysts utilizing rotating disk electrode technique: II. influence of ink formulation, catalyst layer uniformity and thickness. *Journal of The Electrochemical Society* **162**, F1384–F1396 (2015).
- [2] Nie, Y., Li, L. & Wei, Z. Recent advancements in Pt and Pt-free catalysts for oxygen reduction reaction. *Chemical Society Reviews* **44**, 2168–2201 (2015).
- [3] Fu, C. *et al.* DFT calculations: A powerful tool for better understanding of electrocatalytic oxygen reduction reactions on Pt-based metallic catalysts. *Computational Materials Science* **170**, 109202 (2019).
- [4] Hua, M., Tian, X., Li, S. & Lin, X. PdAg/Ag(111) surface alloys: A highly efficient catalyst of oxygen reduction reaction. *Nanomaterials* **12**, 1802 (2022).
- [5] Yarlagadda, V. *et al.* Preparation of PEMFC electrodes from milligram-amounts of catalyst powder. *Journal of The Electrochemical Society* **164**, F845–F849 (2017).
- [6] Kocha, S. S. *et al.* Best practices and testing protocols for benchmarking ORR activities of fuel cell electrocatalysts using rotating disk electrode. *Electrocatalysis* **8**, 366–374 (2017).
- [7] Shinozaki, K. *et al.* Oxygen reduction reaction activity measurement for fuel cell catalysts using the rotating disk electrode technique. *R&D Rev. Toyota CRDL* **49**, 33–46 (2018).
- [8] Chen, G. *et al.* Evaluation of oxygen reduction activity by the thin-film rotating disk electrode methodology: the effects of potentiodynamic parameters. *Electrocatalysis* **7**, 305–316 (2016).
- [9] Du, C., Tan, Q., Yin, G. & Zhang, J. *Rotating Electrode Methods and Oxygen Reduction Electrocatalysts*, Ch. 5, 171–198 (Elsevier, 2014).
- [10] Du, C., Sun, Y., Shen, T., Yin, G. & Zhang, J. *Applications of RDE and RRDE methods in oxygen reduction reaction*, Ch. 7, 231–277 (Elsevier, 2014).
- [11] Douglin, J. C. *et al.* High-performance ionomerless cathode anion-exchange membrane fuel cells with ultra-low-loading Ag–Pd alloy electrocatalysts. *Nature Energy*

- 8, 1262–1272 (2023).
- [12] Stamenkovic, V. R. *et al.* Improved oxygen reduction activity on pt₃ni (111) via increased surface site availability. *Science* **315**, 493–497 (2007).
- [13] Masa, J., Batchelor-McAuley, C., Schuhmann, W. & Compton, R. G. Koutecky-levich analysis applied to nanoparticle modified rotating disk electrodes: Electrocatalysis or misinterpretation. *Nano Research* **7**, 71–78 (2014).
- [14] Martín, A., Chaparro, A., Folgado, M., Rubio, J. & Daza, L. Rotating disk electrode analysis of oxygen reduction at platinum particles under limiting diffusion conditions. *Electrochimica acta* **54**, 2209–2217 (2009).
- [15] Kreider, M. E. *et al.* Strategies for modulating the catalytic activity and selectivity of manganese antimonates for the oxygen reduction reaction. *ACS Catalysis* **12**, 10826–10840 (2022).
- [16] Shinozaki, K., Zack, J. W., Pylypenko, S., Pivovar, B. S. & Kocha, S. S. Oxygen reduction reaction measurements on platinum electrocatalysts utilizing rotating disk electrode technique: Ii. influence of ink formulation, catalyst layer uniformity and thickness. *Journal of The Electrochemical Society* **162**, F1384–F1396 (2015).
- [17] Deschamps, F. L., Mahy, J. G., Leonard, A. F. & Job, N. Rotating disk electrode measurements on low and high loading catalyst layers: Diffusion limitations and application to pt catalysts supported on porous micrometric carbon xerogel particles designed for proton exchange membrane fuel cells. *Journal of Electroanalytical Chemistry* **933**, 117279 (2023).
- [18] Garsany, Y., Ge, J., St-Pierre, J., Rocheleau, R. & Swider-Lyons, K. E. Analytical procedure for accurate comparison of rotating disk electrode results for the oxygen reduction activity of pt/c. *Journal of The Electrochemical Society* **161**, F628–F640 (2014).
- [19] Kokhanov, A. A. *et al.* Improving the reproducibility of oxygen reduction reaction activity assessment for pt-based electrocatalysts on a rotating disk electrode via catalytic layer optimization. *Catalysts* **15**, 1140 (2025).
- [20] Knoche, K. L., Hettige, C., Zook-Gerdau, L. A. & Leddy, J. Film permeation by rotating disk voltammetry at electrodes modified with electrochemically inert

- layers and heterogeneous composites. *Journal of The Electrochemical Society* **163**, H3173–H3181 (2016).
- [21] Xu, S. *et al.* Building upon the koutecky-levich equation for evaluation of next-generation oxygen reduction reaction catalysts. *Electrochimica Acta* **255**, 99–108 (2017).
- [22] Bonnacaze, R. T., Mano, N., Nam, B. & Heller, A. On the behavior of the porous rotating disk electrode. *Journal of the Electrochemical Society* **154**, F44–F47 (2007).
- [23] Deo, S. *et al.* Interpretable machine learning models for practical antimonate electrocatalyst performance. *ChemPhysChem* **25**, e202400010 (2024).
- [24] Lazaridis, T., Stühmeier, B. M., Gasteiger, H. A. & El-Sayed, H. A. Capabilities and limitations of rotating disk electrodes versus membrane electrode assemblies in the investigation of electrocatalysts. *Nature Catalysis* **5**, 363–373 (2022).
- [25] Dull, S. M. *et al.* Alloyed pt–zn oxygen reduction catalysts for proton exchange membrane fuel cells. *ACS Applied Energy Materials* **5**, 8282–8291 (2022).
- [26] Chen, W. *et al.* Reconsidering the benchmarking evaluation of catalytic activity in oxygen reduction reaction. *IScience* **23** (2020).
- [27] Fan, J. *et al.* Bridging the gap between highly active oxygen reduction reaction catalysts and effective catalyst layers for proton exchange membrane fuel cells. *Nature Energy* **6**, 475–486 (2021).
- [28] Zaman, S., Tian, X. & Xia, B. Y. Bridging oxygen reduction performance gaps in half and full cells: Challenges and perspectives. *Materials Chemistry Frontiers* **7**, 4605–4612 (2023).
- [29] Pearl, J. *Causality* (Cambridge university press, 2009).
- [30] Halpern, J. Y. *Actual causality* (MiT Press, 2016).
- [31] Klebel, T. & Traag, V. Introduction to structural causal models in science studies. *Quantitative Science Studies* **7**, 159–178 (2026).

- [32] Friston, K. Causal modelling and brain connectivity in functional magnetic resonance imaging. *PLoS biology* **7**, e1000033 (2009).
- [33] Motevalli, B., Sun, B. & Barnard, A. S. Understanding and predicting the cause of defects in graphene oxide nanostructures using machine learning. *The Journal of Physical Chemistry C* **124**, 7404–7413 (2020).
- [34] Ghosh, A. & Ghosh, S. Mapping causal pathways with structural modes fingerprint for perovskite oxides. *Machine Learning: Science and Technology* **5**, 045014 (2024).
- [35] Barakati, K. *et al.* Mapping causal patterns in crystalline solid. *APL Machine Learning* **3** (2025).
- [36] Kalinin, S. V., Ghosh, A., Vasudevan, R. & Ziatdinov, M. From atomically resolved imaging to generative and causal models. *Nature Physics* **18**, 1152–1160 (2022).
- [37] Witty, S. A. *Bayesian Structural Causal Inference with Probabilistic Programming*. Ph.D. thesis, Ph. D. Dissertation. University of Massachusetts Amherst (2023).
- [38] Aykol, M. *et al.* Perspective—combining physics and machine learning to predict battery lifetime. *Journal of The Electrochemical Society* **168**, 030525 (2021).
- [39] Tran, K. *et al.* Methods for comparing uncertainty quantifications for material property predictions. *Machine Learning: Science and Technology* **1**, 025006 (2020).
- [40] Kutner, M. H. *et al.* *Applied linear statistical models* (India McGraw-Hill Education, 1984).
- [41] Vehtari, A., Simpson, D., Gelman, A., Yao, Y. & Gabry, J. Pareto smoothed importance sampling. *Journal of Machine Learning Research* **25**, 1–58 (2024).
- [42] Dang, L. E. *et al.* A causal roadmap for generating high-quality real-world evidence. *Journal of Clinical and Translational Science* **7**, e212 (2023).
- [43] Gelman, A. *et al.* Bayesian workflow. *arXiv preprint arXiv:2011.01808* (2020).

- [44] Lind, M. *Multilevel flow modelling of process plant for diagnosis and control* (Risø National Laboratory, 1982).
- [45] Rosenberg, R. Exploiting bond graph causality in physical system models. *Journal of Dynamic Systems, Measurement, and Control* (1987).
- [46] Gridin, V. *et al.* Gde vs rde: Impact of operation conditions on intrinsic catalytic parameters of fenc catalyst for the oxygen reduction reaction. *Electrochimica Acta* **444**, 142012 (2023).
- [47] Darab, M., Barnett, A. O., Lindbergh, G., Thomassen, M. S. & Sunde, S. The influence of catalyst layer thickness on the performance and degradation of pem fuel cell cathodes with constant catalyst loading. *Electrochimica acta* **232**, 505–516 (2017).
- [48] Rao, V. *et al.* The influence of carbon support porosity on the activity of ptu/sibunit anode catalysts for methanol oxidation. *Journal of Power Sources* **145**, 178–187 (2005).
- [49] Gong, Q. *et al.* Effects of ink formulation on construction of catalyst layers for high-performance polymer electrolyte membrane fuel cells. *ACS applied materials & interfaces* **13**, 37004–37013 (2021).
- [50] Li, C. *et al.* Effects of ink formulation on the structure and performance of pgm-free catalyst layer in pemfcs. *Electrochemical Society Transactions 240* **104**, 327–333 (2021).
- [51] Su, Y. *et al.* Bridging ink formulation and proton exchange membrane fuel cell performance: Deciphering the role of catalyst ink composition in regulating ionomer behaviors and aggregates/agglomerates structures for high performance cell design. *Renewable and Sustainable Energy Reviews* **225**, 116163 (2026).
- [52] Singh, R. K., Devivaraprasad, R., Kar, T., Chakraborty, A. & Neergat, M. Electrochemical impedance spectroscopy of oxygen reduction reaction (orr) in a rotating disk electrode configuration: effect of ionomer content and carbon-support. *Journal of The Electrochemical Society* **162**, F489–F498 (2015).
- [53] Pearl, J. in *Direct and indirect effects* (eds Geffner, H., Dechter, R. & Halpern, J. Y.) *Probabilistic and causal inference: the works of Judea Pearl* 373–392

(Association for Computing Machinery, New York, NY, USA, 2022).

- [54] Hoffman, M. D., Blei, D. M., Wang, C. & Paisley, J. Stochastic variational inference. *Journal of machine learning research* (2013).
- [55] Institute, B. R. Chirho. <https://github.com/BasisResearch/chirho> (2025). V0.3.0.
- [56] Xu, X. *et al.* Toward enhanced pyro-catalysis performance: mechanisms, strategies and challenges. *Journal of Materials Chemistry A* **13**, 14465–14490 (2025).
- [57] Paszke, A. *et al.* Pytorch: An imperative style, high-performance deep learning library. *Advances in neural information processing systems* **32** (2019).
- [58] Paszke, A. *et al.* Automatic differentiation in pytorch. NIPS 2017 Autodiff Workshop (2017).